Fracture analysis of thin films on compliant substrates: a numerical study using the phase field approach of fracture

T. Guillén-Hernández[a,b], J. Reinoso[b,*], M. Paggi[a]

[a] *IMT Institute for Advanced Studies Lucca, Piazza San Francesco 19, 55100, Lucca, Italy*
[b] *Elasticity and Strength of Materials Group, School of Engineering. Universidad de Sevilla, Camino de los Descubrimientos s/n, 41092, Seville, Spain*

Abstract

In this work, the phase field (PF) approach for brittle fracture in the bulk coupled with the cohesive zone model (CZM) for pre-existing interfaces is exploited for the simulation of fracture of thin films on compliant substrates, which are structural configurations of extensive use in many engineering systems such as protecting layers for vessels, stretchable electronic devices, among many others. Due to the coupling between the two aforementioned models for fracture, the proposed approach enables capturing bulk damage and crack deflection or penetration at the prescribed interfaces in a robust and reliable manner, these scenarios depending on the particular mechanical properties of the system under analysis via a sensitivity analysis. In this concern, it is shown that the proposed approach is capable of predicting several complex crack paths for different fracture modes, concerning the 2D and 3D thin film fracture problems herein investigated: (i) deflection/delamination, (ii) penetration and (iii) deflection/delamination at the prescribed interface in combination with penetration. Moreover, the effect of the interface fracture energy on the predicted crack path has been carefully investigated.

Keywords: Phase Field approach to fracture; Thin Film; Cohesive Zone Model; Crack penetration; Crack deflection; Shell finite elements

1. Introduction

Coatings and thin films supported on compliant substrates can experience different fracture events, which can limit the performance and mechanical integrity of the corresponding engineering systems. Practical applications of thin film-substrate components can be found in many engineering products ranging from thermal barrier coatings, renewable energy systems to vessels, among others.

In order to achieve a deep understanding of thin film-substrate designs, numerous studies have been carried out in the last three decades through analytical, experimental and numerical methods (mostly using the nonlinear finite element method, FEM). The complexity of these systems provokes the appearance of multiple fracture patterns as a consequence of the notable elastic mismatch of the constituents. Within the framework of Linear Elastic Fracture Mechanics (LEFM), Hutchison and coauthors [1, 2] provided an overall picture with regard to the energy release rate associated with penetration-deflection scenarios for general layered materials, whose fundamental results have been later recalled in [3, 4, 5] and the references given therein. Numerically, many recent investigations prolifically dealt with the use of cohesive zone models [6, 7] for triggering delamination events in thin layer-substrate systems, whereby inelastic processes due to fracture have been mostly confined to the interface between the composing parts [8, 9].

Owing to its widespread use in many engineering products, the reliable prediction of failure mechanisms from different signature in heterogenous systems is of great importance. In this setting, the phase field (PF)

*Corresponding authors
Email address: jreinoso@us.es (J. Reinoso)

approach to fracture offers different appealing aspects in situations comprising complex crack topologies such coalescence and branching, among other scenarios, and enables overcoming some of the most remarkable limitations of discontinuity-based methods [10, 11]. The basic concept of the PF approach encompasses a diffusive crack representation based on the introduction of the crack phase field variable $\mathfrak{d}$, with $\mathfrak{d} : \mathcal{B}_t \in [0,t] \longrightarrow [0,1]$ [12, 13], where $\mathcal{B}_t \in \mathbb{R}^n$ denotes the domain of an arbitrary body in the Euclidean space, whose material position vectors are identified by $\mathbf{x}$. The PF formulation can be conceived as a nonlocal model suitable for brittle and ductile fracture, and whose essential concepts are rooted in Fracture Mechanics. This concerns the consideration of a crack density functional which depends on $\mathfrak{d}$, its gradient $\nabla_{\mathbf{x}}\mathfrak{d}$ and the length scale l [14] (Fig. 1.a):

$$\gamma(\mathfrak{d}, \nabla_{\mathbf{x}}\mathfrak{d}) = \frac{1}{2l}\mathfrak{d}^2 + \frac{l}{2}|\nabla_{\mathbf{x}}\mathfrak{d}|^2. \tag{1}$$

.

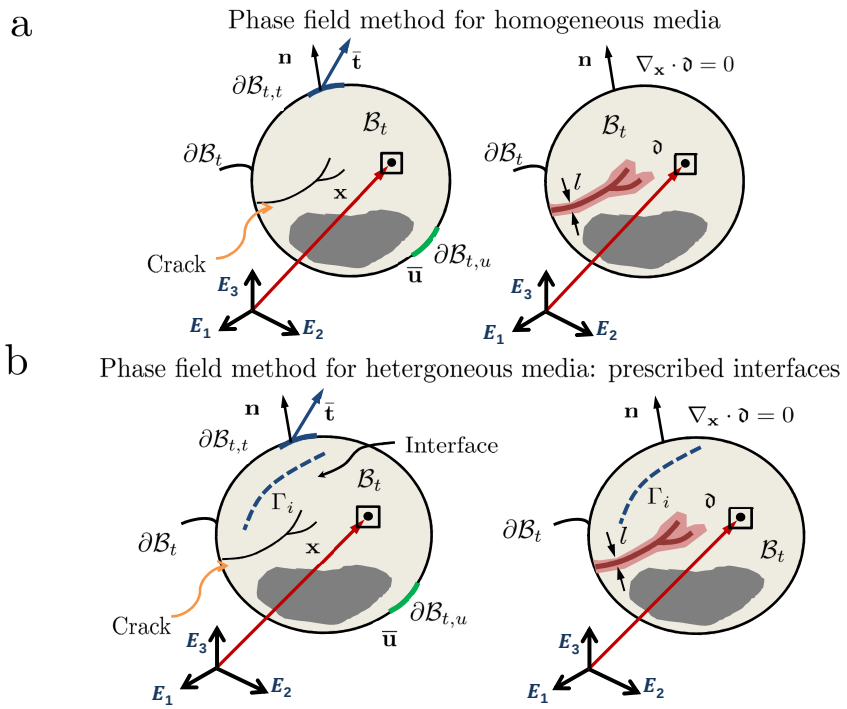

Figure 1: (a) General modeling framework of the PF approach of fracture using the diffusive crack concept within a region of width l. (b) Heterogeneous cracked systems with prescribed interfaces: basis of the PF-CZ method.

The functional $\gamma(\mathfrak{d}, \nabla_{\mathbf{x}}\mathfrak{d})$ provides the starting point of the PF approach for fracture owing to the fact that it allows approximating surface integrals on sharp crack surfaces $\Gamma_c \in \Omega$ by volume integrals. Therefore, the dissipative part of the original Griffith's functional can be rephrased as [15]:

$$\int_{\Gamma_c} \mathcal{G}_c \, \mathrm{d}\partial\Omega \approx \int_{\mathcal{B}_t} \mathcal{G}_c \gamma(\mathfrak{d}, \nabla_{\mathbf{X}}\mathfrak{d}) \, \mathrm{d}\Omega, \tag{2}$$

where $\mathcal{G}_c$ is the fracture toughness according to the Griffith fracture theory. Thus, the total potential energy of the system renders

$$\Pi(\mathbf{u}, \mathfrak{d}) = \int_{\mathcal{B}_t} \psi(\boldsymbol{\varepsilon}, \mathfrak{d}) \, \mathrm{d}\Omega + \int_{\mathcal{B}_t} \mathcal{G}_c \gamma(\mathfrak{d}, \nabla_{\mathbf{x}}\mathfrak{d}) \, \mathrm{d}\Omega, \tag{3}$$

where $\psi(\boldsymbol{\varepsilon}, \mathfrak{d})$ stands the elastic energy density which depends on the damage $\mathfrak{d}$ and the strain $\boldsymbol{\varepsilon}$.

As a consequence of its versatility, the PF approach has attracted a remarkable attention over the last decade, leading to a wide variety of developments focused on dynamic fracture [16], thermo-mechanical applications [17, 18], fracture in shells [19, 20, 21], hydrogen assisted cracks [22] and many others. In this setting, the authors seminally proposed a modeling framework for triggering fracture events in heterogeneous media encompassing different materials, whereby the existing interfaces play a major role. This novel computational methodology couples the PF approach for bulk fracture and interface-like models (cohesive zone model, CZM) for delamination events in a consistent and modular form, being called as PF-CZM technique. The reliability of this seminal method was thoroughly examined in [23] through retrieving fundamental LEFM results, whilst its versatility has been examined by means of the application of this concept to Silicon based polycrystal materials [24], layered ceramics [25, 26], among other applications.

In view of the strong potential of the combined PF-CZM methodology, this paper analyzes crack events in thin film-substrate systems subjected to tensile stresses, with the aim of gaining a more profound understanding of the failure mechanisms that interplay in their designs.

2. Computational strategy: coupled phase field of fracture and cohesive-like interface approach for heterogeneous media

This section succinctly presents the main aspects of the coupled phase field approach to fracture and cohesive-like interface models for heterogeneous media developed in [23]. Within the scope of the current study, we present the variational formalisms of the PF-CZM method for 2D small strains and 3D large strains for solid shells in Sects. 2.1 and 2.2, respectively. Particular developments with regard to the corresponding FE implementations are omitted in the sequel for the sake of brevity, see [21, 26, 25] for further details.

2.1. Modeling framework for 2D systems in the infinitesimal deformation setting

The point of departure of the current numerical method is the consideration of a generic crack body with prescribed interfaces Γ_i ((Fig. 1.b)). The material points of the bulk are identified by the position vectors $\mathbf{x}$, whereas the points on the interface Γ_i are given by the vector $\mathbf{x}_c$. For the separated treatment of the energy that is dissipated within the bulk and along the interfaces, it is assumed that the free energy functional which governs the mechanics of the body Ω, Eq. (3), can be rephrased as

$$\Pi(\mathbf{u},\Gamma_b,\Gamma_i) = \Pi_\Omega + \Pi_{\Gamma_b} + \Pi_{\Gamma_i} = \int_{\mathcal{B}_t\setminus\Gamma} \psi^e(\boldsymbol{\varepsilon})\,\mathrm{d}\Omega + \int_{\Gamma_b} \mathcal{G}_c^b(\mathbf{u},\mathfrak{d})\,\mathrm{d}\Gamma + \int_{\Gamma_i} \mathcal{G}^i\left(\mathbf{g},\mathfrak{h},\mathfrak{d}\right)\,\mathrm{d}\Gamma, \tag{4}$$

where $\mathbf{g}$ stands for the displacement jump between the interface flanks, $\mathfrak{h}$ is an interface history parameter [27], and $\mathfrak{d}$ denoted the phase field variable. In Eq.(4), the central idea of the proposed method concerns the additive split the fracture energy function $\mathcal{G}_c$ that can be released in the system into the following contributions: (i) $\mathcal{G}_c^b$ describing the fracture in the bulk, which is modeled via the PF approach, and (ii) $\mathcal{G}^i$ which endows the delamination failure along the prescribed interfaces in the system, this phenomena being simulated using the so-called CZM. At this point, it is worth mentioning that the current approach introduces the consideration of two length scales as was thoroughly analyzed in [23], i.e the phase field l and the cohesive-like crack l_{CZM} length scales.

Through the invocation of the PF approach for the bulk, Eq.(5) renders

$$\Pi(\mathbf{u},\mathfrak{d}) = \Pi_b + \Pi_{\Gamma_i} = \int_{\mathcal{B}_t} \psi(\boldsymbol{\varepsilon},\mathfrak{d})\,\mathrm{d}\Omega + \int_{\mathcal{B}_t} \mathcal{G}_c^b \gamma(\mathfrak{d},\nabla_{\mathbf{x}}\mathfrak{d})\,\mathrm{d}\Omega + \int_{\Gamma_i} \mathcal{G}^i\left(\mathbf{g},\mathfrak{h},\mathfrak{d}\right)\,\mathrm{d}\Gamma, \tag{5}$$

with

$$\Pi_b(\mathbf{u},\mathfrak{d}) = \int_{\mathcal{B}_t} \psi(\boldsymbol{\varepsilon},\mathfrak{d})\,\mathrm{d}\Omega + \int_{\mathcal{B}_t} \mathcal{G}_c^b \gamma(\mathfrak{d},\nabla_{\mathbf{x}}\mathfrak{d})\,\mathrm{d}\Omega; \qquad \Pi_{\Gamma_i}(\mathbf{u}) = \int_{\Gamma_i} \mathcal{G}^i\left(\mathbf{g},\mathfrak{h},\mathfrak{d}\right)\,\mathrm{d}\Gamma. \tag{6}$$

One possible coupling form between the PF approach in the bulk and the CZM along the interface can be accomplished through the tension cut-off interface model [28], which has been also denominated as the Linear Elastic Interface Model (LEBIM) [29]. Recalling, Paggi and Reinoso [23] the effect of the

average bulk damage $\mathfrak{d}$ of the continuum surrounding the interface flanks is accounted for by means of modifying the apparent interface stiffness. Thus, the critical opening displacement of the CZM (g_c) obeys a linear dependence upon the bulk damage $\mathfrak{d}$: $g_c(\mathfrak{d}) = (1-\mathfrak{d})g_{c,0} + \mathfrak{d}g_{c,1}$, where $g_{c,0} = g_c(\mathfrak{d}=0)$ stands for the critical gap for intact bulk, whereas $g_{c,1} = g_c(\mathfrak{d}=1)$ identifies the critical gap for fully deteriorated surrounding bulk. This relationship is assumed for the cohesive traction-separation laws corresponding to fracture Mode I and Mode II in the 2D setting, see Fig. 2.a for a generic fracture mode. Mathematically, the corresponding interface law for each fracture mode is given by

$$\sigma = \begin{cases} k_n \dfrac{g_n}{g_{nc}}, & \text{if } 0 < \dfrac{g_n}{g_{nc}} < 1; \\ 0, & \text{if } \dfrac{g_n}{g_{nc}} \geq 1, \end{cases} \tag{7}$$

$$\tau = \begin{cases} k_t \dfrac{g_t}{g_{tc}}, & \text{if } 0 < \dfrac{g_t}{g_{tc}} < 1; \\ 0, & \text{if } \dfrac{g_t}{g_{tc}} \geq 1. \end{cases} \tag{8}$$

where σ and τ identify the Mode I and Mode II traction components, respectively, g is the relative displacement, and the subscript n and t refers to Mode I and Mode II deformation, respectively.

Accordingly, the generic stiffness of the cohesive law k depends on the phase field crack variable $\mathfrak{d}$:

$$k_n = k_{n,0}\left(\frac{g_{nc,0}}{g_{nc}}\right)^2; \quad k_t = k_{t,0}\left(\frac{g_{tc,0}}{g_{tc}}\right)^2, \tag{9}$$

where k_0 and g_0 are the stiffness and critical relative displacement for $\mathfrak{d}=0$.

Finally, and without loss of generality, interface failure is attained using a mixed mode quadratic criterion:

$$\left(\frac{\mathcal{G}_I^i}{\mathcal{G}_{IC}^i}\right)^2 + \left(\frac{\mathcal{G}_{II}^i}{\mathcal{G}_{IIC}^i}\right)^2 = 1, \tag{10}$$

where $\mathcal{G}_I^i$ and $\mathcal{G}_{II}^i$ are the energy release rates for fracture Mode I and Mode II, respectively, which are given by

$$\mathcal{G}_I^i(\mathfrak{d}) = \frac{1}{2}k_{n,0}g_n^2\frac{g_{nc,0}^2}{[(1-\mathfrak{d})g_{nc,0}+\mathfrak{d}g_{nc,1}]^2}; \quad \mathcal{G}_{II}^i(\mathfrak{d}) = \frac{1}{2}k_{t,0}g_t^2\frac{g_{tc,0}^2}{[(1-\mathfrak{d})g_{tc,0}+\mathfrak{d}g_{tc,1}]^2}. \tag{11}$$

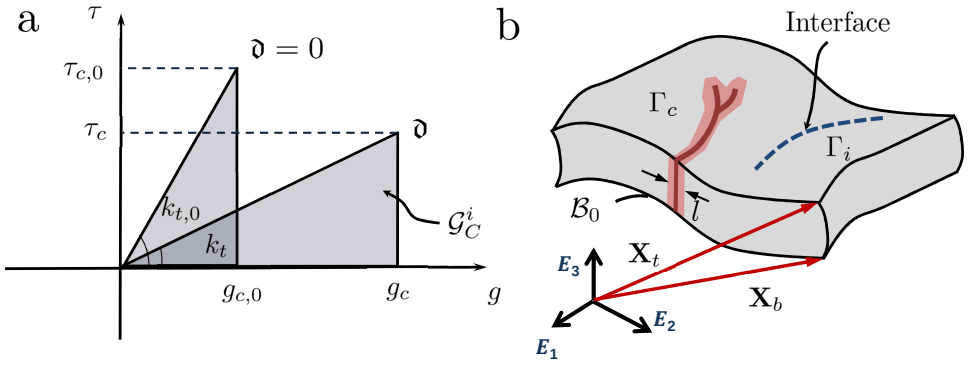

Figure 2: (a) General fracture mode: traction-separation law based on a tension cut-off interface compatible with the PF approach of fracture in the bulk. (b) Cracked shell with presence of prescribed interfaces.

2.2. Modeling framework for 3D systems in the large deformation setting: particularization to enhanced-assumed solid shell elements

This section summarizes the extension of the modeling approach described in the previous section for 3D large strains applications incorporating a nonlinear enhanced assumed solid shell model into the formulation.

This shell model is especially suitable for triggering fracture events in thin walled structures, displaying a locking free performance from the numerical standpoint [21, 30, 31].

For nonlinear shell analysis undergoing large deformations, we denote $\mathcal{B}_0 \subset \mathbb{R}^3$ as the reference placement and $\mathcal{B}_t \subset \mathbb{R}^3$ its corresponding current placement. The position vectors at the reference and current configurations are denoted by $\mathbf{X}$ and $\mathbf{x}$, respectively. The nonlinear deformation mapping is defined as: $\boldsymbol{\varphi}(\mathbf{X}, t) : \mathcal{B}_0 \times [0, t] \to \mathbb{R}^3$, where $[0, t]$ stands for the time step interval mapping the reference material points ($\mathbf{X} \in \mathcal{B}_0$) onto the current material points ($\mathbf{x} \in \mathcal{B}_t$), such that $\mathbf{x} = \boldsymbol{\varphi}(\mathbf{X}, t)$. The definition of the displacement-derived deformation renders: $\mathbf{F}^u := \partial_{\mathbf{X}} \boldsymbol{\varphi}(\mathbf{X}, t)$, where $J^u = \det[\mathbf{F}^u]$ is the corresponding Jacobian of the transformation, and $\partial_{\mathbf{X}}$ is the partial derivative with respect to the reference frame.

The parametric space identified for the current shell model is denoted as: $\mathcal{A} := \{\boldsymbol{\xi} = (\xi^1, \xi^2, \xi^3) \in \mathbb{R}^3 \mid -1 \leq \xi^i \leq +1; i = 1, 2, 3\}$, where (ξ^1, ξ^2) are in-plane directions, ξ^3 stands for the thickness direction and H is the initial shell thickness. The solid shell formulation, also denominated as 6-parameter shell model, envisages the parametrization of an arbitrary material point $\mathbf{X}(\boldsymbol{\xi})$ through the linear interpolation of the position of the top $\mathbf{X}_t(\xi^1, \xi^2)$ and bottom $\mathbf{X}_b(\xi^1, \xi^2)$ vectors:

$$\mathbf{X}(\boldsymbol{\xi}) = \frac{1}{2}\left(1 + \xi^3\right)\mathbf{X}_t(\xi^1, \xi^2) + \frac{1}{2}\left(1 - \xi^3\right)\mathbf{X}_b(\xi^1, \xi^2). \tag{12}$$

This interpolation scheme also holds for the current configuration:

$$\mathbf{x}(\boldsymbol{\xi}) = \frac{1}{2}\left(1 + \xi^3\right)\mathbf{x}_t(\xi^1, \xi^2) + \frac{1}{2}\left(1 - \xi^3\right)\mathbf{x}_b(\xi^1, \xi^2). \tag{13}$$

The kinematics field, $\mathbf{u}(\boldsymbol{\xi})$ yields

$$\mathbf{u}(\boldsymbol{\xi}) := \mathbf{x}(\boldsymbol{\xi}) - \mathbf{X}(\boldsymbol{\xi}) = \mathbf{v}(\xi^1, \xi^2) + \xi^3 \mathbf{w}(\xi^1, \xi^2) \tag{14}$$

where $\mathbf{v}(\xi^1, \xi^2)$ and $\mathbf{w}(\xi^1, \xi^2)$ stand for the displacement of the shell midsurface and the displacement vector that accounts for the difference between the shell director vector in the reference and in the current configuration, respectively. The co-variant basis in the reference ($\mathbf{G}_i$) and current ($\mathbf{g}_i$) configurations render

$$\mathbf{G}_i(\boldsymbol{\xi}) := \frac{\partial \mathbf{X}(\boldsymbol{\xi})}{\partial \xi^i}, \qquad \mathbf{g}_i(\boldsymbol{\xi}) := \frac{\partial \mathbf{x}(\boldsymbol{\xi})}{\partial \xi^i}, \tag{15}$$

whereas in the curvilinear setting the displacement derived deformation gradient, $\mathbf{F}^u$, takes the form

$$\mathbf{F}^u := \mathbf{g}_i \otimes \mathbf{G}^i. \tag{16}$$

The previous parametrization is also assumed for the phase field variable, identifying the phase field variables corresponding to the top and bottom surfaces of the shell, $\mathfrak{d}_t$ and $\mathfrak{d}_b$, respectively [21]:

$$\mathfrak{d}(\boldsymbol{\xi}) = \frac{1}{2}\left(1 + \xi^3\right)\mathfrak{d}_t(\xi^1, \xi^2) + \frac{1}{2}\left(1 - \xi^3\right)\mathfrak{d}_b(\xi^1, \xi^2). \tag{17}$$

With regard to the variational formalism, in the current solid shell formulation, the enhanced assumed strain (EAS) technology is advocated to alleviate locking pathologies. In particular, the EAS method is adopted through the additive decomposition of the Green-Lagrange strain tensor $\mathbf{E} = \mathbf{E}^u + \tilde{\mathbf{E}}$, where $\mathbf{E}^u$ and $\tilde{\mathbf{E}}$ denote the compatible and the incompatible counterparts of the strain [32, 33], respectively. In this concern, the formulation is defined through the Hu-Washizu functional, whereby the displacements $\mathbf{u}$, the incompatible strains $\tilde{\mathbf{E}}$, the second Piola-Kirchhoff stress tensor $\mathbf{S}$, and the crack phase field variable $\mathfrak{d}$ constitute the independent fields of the formulation.

Considering a generic shell with cracks and a pre-existing interface as shown in Fig. 2.b, the dissipative part of the energy functional is again split into a bulk contribution and an interface contribution (Eq. (4)). This split is introduced in the Hu-Washizu functional leading to the following expression:

$$\Pi(\mathbf{u}, \tilde{\mathbf{E}}, \mathbf{S}, \mathfrak{d}) = \int_{\mathcal{B}_0 \setminus \Gamma} \mathfrak{g}(\mathfrak{d}) \Psi(\mathbf{E}) \, \mathrm{d}\Omega - \int_{\mathcal{B}_0} \mathbf{S} : \tilde{\mathbf{E}} \, \mathrm{d}\Omega + \underbrace{\int_{\mathcal{B}_0} \mathcal{G}_c^b \gamma(\mathfrak{d}, \nabla_{\mathbf{X}} \mathfrak{d}) \, \mathrm{d}\Omega}_{\Pi_{\mathrm{fr}}^b} + \underbrace{\int_{\Gamma_i} \mathcal{G}_c^i(\mathbf{u}, \mathfrak{d}) \, \mathrm{d}\Gamma}_{\Pi_{\mathrm{fr}}^i} + \Pi_{\mathrm{ext}}, \tag{18}$$

where $\Pi^b_{\rm fr}$ is the bulk contribution and $\Pi^i_{\rm fr}$ is the interface-related term, whereas $\Pi_{\rm ext}$is the external potential.

Differing from the previous 2D small strain formulation formulation, it is notable to remak that the extension to 3D cases requires the introduction of the fracture Mode III within the proposed framework and the computation of the linearizarion of the rotation operator with respect to the displacement field as was detailed in [7]. Then, the constitutive response for a generic fracture Mode reads:

$$S_m = \begin{cases} k_m \dfrac{g_m}{g_{m,c}}, & \text{if } 0 < \dfrac{g_m}{g_{m,c}} < 1; \qquad \text{with} \quad m = n, t1, t2 \\ 0, & \text{if } \dfrac{g_m}{g_{m,c}} \geq 1, \end{cases} \tag{19}$$

where S_m identifies the Piola stress of the interface, being $S_{m,c}$ its corresponding critical value; k_m is the interface stiffness, whereas g_m and $g_{m,c}$ are the displacement gap and its critical value in the local reference system of the interface. The previous cohesive law is further equipped with a penalty formulation in compression with the aim of precluding the material interpenetration at the interface.

Relying on the these considerations, the fracture energies for a generic fracture Mode are:

$$\mathcal{G}^i_{m,c} = \frac{1}{2} S_m g_{m,c} = \frac{1}{2} k_m g^2_{m,c}. \qquad \text{with} \quad m = n, t1, t2 \tag{20}$$

Similarly to the 2D case, the critical relative displacements triggering interface failure have a linear dependence on $\hat{\mathfrak{d}}$. On the contrary, the critical energy release rate for each fracture Mode is preserved throughout the corresponding analysis. Then, imposing the independence of the fracture energies for each Mode and the crack phase field value, the following expressions for the energy release rates are derived:

$$\mathcal{G}^i_m(\mathfrak{d}) = \frac{1}{2} k_{m,0} g^2_m \frac{g^2_{m,c,0}}{\left[(1-\mathfrak{d}) g_{m,c,0} + \mathfrak{d} g_{m,c,1}\right]^2}. \qquad \text{with} \quad m = n, t1, t2 \tag{21}$$

Without loss of generality, a standard quadratic criterion to trigger the interface failure under Mixed Mode fracture conditions is again adopted as in 2D and it reads:

$$\left(\frac{\mathcal{G}^i_n}{\mathcal{G}^i_{n,C}}\right)^2 + \left(\frac{\mathcal{G}^i_{t1}}{\mathcal{G}^i_{t1,C}}\right)^2 + \left(\frac{\mathcal{G}^i_{t2}}{\mathcal{G}^i_{t2,C}}\right)^2 = 1. \tag{22}$$

Finally, the following tangent constitutive operators at the interface are derived for the subsequent numerical treatment via nonlinear FEM:

$$\frac{\partial^2 \mathcal{G}^i_c}{\partial \mathbf{g}^2_{\rm loc}} = \begin{bmatrix} \hat{\alpha} k_n & 0 & 0 \\ 0 & \hat{\beta} k_{t1} & 0 \\ 0 & 0 & \hat{\gamma} k_{t2} \end{bmatrix}, \tag{23a}$$

$$\frac{\partial^2 \mathcal{G}^i_c}{\partial \mathbf{g}_{\rm loc} \partial \hat{\mathfrak{d}}} = \begin{bmatrix} g_n k_n \dfrac{\partial \hat{\alpha}}{\partial \hat{\mathfrak{d}}} & g_{t1} k_{t1} \dfrac{\partial \hat{\beta}}{\partial \hat{\mathfrak{d}}} & g_{t2} k_{t2} \dfrac{\partial \hat{\gamma}}{\partial \hat{\mathfrak{d}}} \end{bmatrix}, \tag{23b}$$

$$\frac{\partial^2 \mathcal{G}^i_c}{\partial \hat{\mathfrak{d}} \partial \mathbf{g}_{\rm loc}} = \begin{bmatrix} g_n k_n \dfrac{\partial \hat{\alpha}}{\partial \hat{\mathfrak{d}}} \\ g_{t1} k_{t1} \dfrac{\partial \hat{\beta}}{\partial \hat{\mathfrak{d}}} \\ g_{t2} k_{t2} \dfrac{\partial \hat{\gamma}}{\partial \hat{\mathfrak{d}}} \end{bmatrix}, \tag{23c}$$

$$\frac{\partial^2 \mathcal{G}^i_c}{\partial \delta \hat{\mathfrak{d}}^2} = \frac{1}{2} g^2_n k_n \frac{\partial^2 \hat{\alpha}}{\partial \hat{\mathfrak{d}}^2} + \frac{1}{2} g^2_{t1} k_{t1} \frac{\partial^2 \hat{\beta}}{\partial \hat{\mathfrak{d}}^2} + \frac{1}{2} g^2_{t2} k_{t2} \frac{\partial^2 \hat{\gamma}}{\partial \hat{\mathfrak{d}}^2}. \tag{23d}$$

where the terms $\hat{\alpha}$, $\hat{\beta}$ and $\hat{\gamma}$ are given by:

$$\hat{\alpha} = \frac{g_{nc,0}^2}{\left[(1-\mathfrak{d})g_{nc,0} + \mathfrak{d}g_{nc,1}\right]^2}, \tag{24a}$$

$$\hat{\beta} = \frac{g_{t1c,0}^2}{\left[(1-\mathfrak{d})g_{t1c,0} + \mathfrak{d}g_{t1c,1}\right]^2} \tag{24b}$$

$$\hat{\gamma} = \frac{g_{t2c,0}^2}{\left[(1-\mathfrak{d})g_{t2c,0} + \mathfrak{d}g_{t2c,1}\right]^2}. \tag{24c}$$

3. Applications

In the sequel, we aim at showing the capabilities of the present model to simulate damage in heterogeneous media with the presence of interfaces in thin layer-substrate systems. The main target is providing a characterization of the different damage patterns that can evolve based on the mechanical properties of the system. For this purpose, we present a comprehensive mechanical study endowing the simulation of several examples with different geometries, cracking paths and types of failure. The current methodology has been implemented into the general purpose FE code FEAP, the simulations being conducted under displacement control.

In Sec. 3.1, we simulate a 2D film/substrate system with a single-edge notched under different loading conditions and respective mechanical properties between the constituents. Additionally, we vary the interface properties and after that, we introduce a secondary notch in order to evaluate its influence on the corresponding damage pattern. These actions are performed in order to study the influence of different system parameters on the propagation path and therefore, on the type of failure. Finally, recalling the information of the simulations herein under consideration, we construct a potential failure map of single-edge notched problem, enabling the quick and efficient prediction of the failure type knowing the properties of the system.

Subsequently, Sect. 3.2 exemplarily addresses the capabilities of the current numerical methodology to simulate 3D problems involving thin layer-substrate systems under the concomitant development of the three fracture modes, i.e. Modes I, II and III.

Moreover, as mentioned above, it is worth mentioning that the present numerical method introduces the role of two length scales into the model, l (associated with the PF model) and l_{CZM} (related to the CZM) following the previous notation. After the computation of both length parameters [34, 35] for the material properties under consideration, we noticed that both length scales are of the similar order of magnitude, leading to a real competition between the corresponding failure modes.

3.1. 2D film/substrate system

In this Section, we first analyse the failure and crack propagation of the system shown in Figure 3, whereby we exploit the longitudinal symmetry of the system. The geometry and material parameters are collected in Tables 1 and 2.

L/t	2000	Specimen length/Interface thickness
h/t	25	Coating thickness/Interface thickness
H/t	250	Substrate thickness/Interface thickness
l_c/t	5	Notch length/Interface thickness

Table 1: 2D film/substrate under tension: Geometrical parameters.

In order to determine the influence of the interface properties on the failure of the system, the interface fracture energy for Mode I, $\mathcal{G}_I$, is varied with respect to the baseline value in Table 2. This leads to three different configurations of the system: weak interface ($\mathcal{G}_I$), intermediate interface ($10 \times \mathcal{G}_I$) and tough

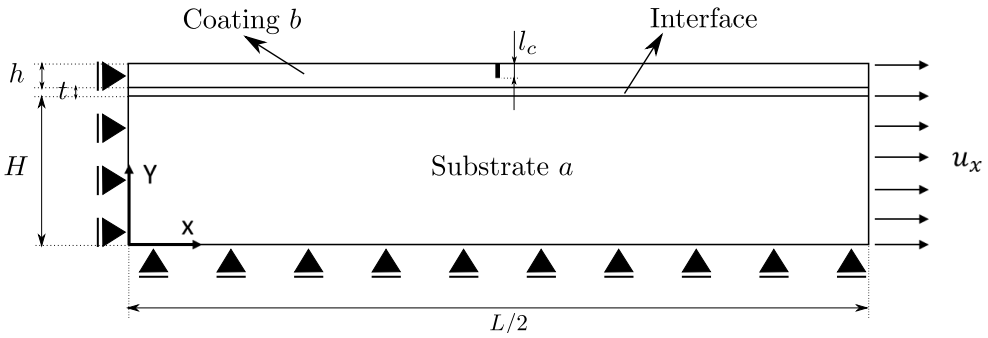

Figure 3: 2D film/substrate under tension: Geometry.

$E_a/\mathcal{G}_a$	1×10^7	Substrate Young modulus/Substrate Fracture energy
$E_b/\mathcal{G}_a$	5×10^8	Coating Young modulus/Substrate Fracture energy
$\nu_a/\mathcal{G}_a$	111	Substrate Poisson ratio /Substrate Fracture energy
$\nu_b/\mathcal{G}_a$	111	Coating Poisson ratio/Substrate Fracture energy
$\mathcal{G}_b/\mathcal{G}_a$	10	Coating Fracture energy/Substrate Fracture energy
$l/\mathcal{G}_a$	83.33	Phase field length scale parameter/Substrate Fracture energy
$\mathcal{G}_I/\mathcal{G}_a$	0.67	Interface Fracture energy for Mode I/Substrate Fracture energy
$\mathcal{G}_{II}/\mathcal{G}_a$	2.67	Interface Fracture energy for Mode II/Substrate Fracture energy
$\sigma_I/\mathcal{G}_a$	25×10^3	Interface Maximum traction for Mode I/Substrate Fracture energy
$\sigma_{II}/\mathcal{G}_a$	30×10^3	Interface Maximum traction for Mode II/Substrate Fracture energy
α	0.96	Dundurs' parameter α
β	0.48	Dundurs' parameter β

Table 2: 2D film/substrate under tension: Mechanical properties.

interface ($100 \times \mathcal{G}_I$). From Figure 4, it can be noticed that for a weak interface, the predominant failure mode is due to pure delamination. However, for the toughest case, the interface represents a very high energetic barrier that is very difficult to break. For this reason, as expected, it is predicted that the crack penetrates into the substrate upon the complete system collapse instead the development of delamination along the prescribed interface. Finally, we analyze an intermediate situation, where the present method estimates the onset and growth of delamination events along the interface until a certain position, following a symmetric pattern, and subsequently these crack events kink out from the interface penetrating into the substrate. These results illustrate one of the main capabilities of the proposed formulation in rather complex damage situations whereby two fracture events from different signature can be efficiently captured without the requirement of any user intervention in order to trigger the crack path throughout the simulations.

It is also worth mentioning that from a quantitative point of view, the dissipated energy in the previous cases is different from each other, according to the stress-strain evolution curves depicted in Figure 4. For instance, in the delamination case, the dissipated energy features the response with the lowest stiffness and dissipating exclusively the energy associated with delamination failure. However, although in the penetration case there is also a single dissipation mechanism, the corresponding crack path is predicted with a larger extent, so the overall dissipated energy is larger with respect to the weakest interface configuration, and therefore leading to stiffer stress-strain response. Finally, for the intermediate case, there are two concomitant dissipation mechanisms (delamination and penetration) which means that, in this case, the dissipated energy corresponds to the toughest configuration. This latter effect can be seen from the secondary branch of the corresponding response after the first drop of the evolution, featuring the system a modified stiffness (governed by the substrate) upon complete failure (second drop in the response).

Note also that although we increase the apparent rigidity of the interface, the overall stiffness of the problem only increases from the weakest interface case to the intermediate one, since the first part of

the evolution prior the first drop is ruled by the thin layer. However, from the intermediate interface case to the tough interface configuration, the stiffness of the problem remains constant but the dissipated energy decreases. This is because, as was discussed above, when the interface is tough enough there is no delamination along the thin layer-substrate interface transferring the imposed actions to the substrate via the joined regions.

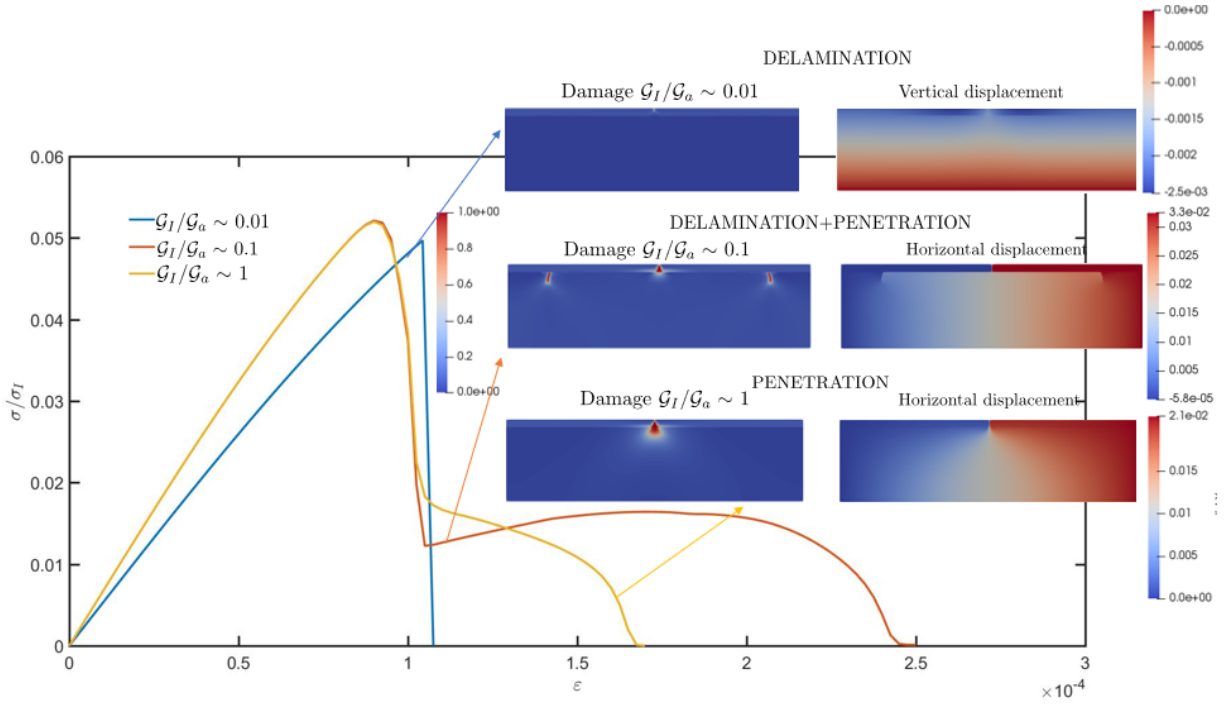

Figure 4: 2D film/substrate under tension problem: Influence of $\mathcal{G}_I$ on the stress-strain evolution curve (stress of the system/stress-layer).

Finally, it is important to remark that current results represent a largely novel contribution to the state-of-the-art regarding the analysis of the characteristic failure mechanisms in thin layer-substrate systems, which are principally confined to fracture aspects around the common interface [36]. Differing from previous investigations, the current approach enables capturing a complete range of damage patterns upon complete system failure.

3.1.1. 2D film/substrate system: analysis of the effect of a secondary notch

Now, we introduce a secondary notch in our problem, close to the previous notch at the center of the system. The distance from the main notch to the secondary one is denoted as h_c, setting: h_c/t=25. We intend illustrating the influence of a secondary notch on the damage patterns and also the role of the interface fracture toughness $\mathcal{G}_I$, as was performed in the previous section. For this purpose, we simulate two problems, each of them corresponding to different values of the secondary notch length: $l_c/2$ and l_c.

The geometry of the problems are given in Figure 5 and the results are shown in Figure 6 and 7.

From these plots note that, in line with the scenarios considering a unique main notch presented above, the system stiffness is ruled by the type of primary failure, i.e. weakest configurations yield to a complete delamination (featuring the most compliant response) whereas intermediate and tough interface cases comply with responses governed by the thin layer stiffness with similar stiffness values up to the first drop in the evolution.

Moreover, analyzing the results obtained from a qualitative standpoint, we can argue that the influence of the secondary notch on the problem response depends on its length. Thus, it can be observed that when

the secondary notch length is equal to $l_c/2$, the results are exactly the same as the results of the one notch problem, i.e with no interactions between notches. However, when the second notch is of the same length as the main one, the predictions are significantly different from the previous examples because there is a clear interaction between the cracks that appear in both notches.

Summarizing current results, the following differences between single and double notched configurations can be identified where there exists interaction between the two notches:

- In the case of weak interfaces, if a secondary flaw is considered, the maximum stress increases with respect to the single notch configuration and the failure happens at lager strain levels but the stiffness system remains constant. This means that we are increasing the dissipated energy. Although there are slight differences in the overall response of the system, the predominant failure is the complete delamination of the thin layer from the substrate.

- For intermediate tough interfaces and two interacting notches, current simulations only predict delamination events for longer secondary notches. Moreover, the failure happens under smaller strain levels in comparison with the single notch specimen. Differing from this, for the double notched system, the maximum stress, the dissipated energy and the stiffness decrease with respect to the single notch system. Stemming from this aspect, it can be stated that the presence of the secondary notch makes weaker the system and causes a different type of failure (delamination instead of delamination followed by penetration).

- Finally, for very tough interfaces, the predicted type of failure does not change between the single and the double notched systems regardless (penetration) the length of the secondary notch. Thus, for systems with two notches and very tough interfaces, in line with weak interface cases, the stiffness remains constant while the dissipated energy increases in comparison with the single notch configurations.

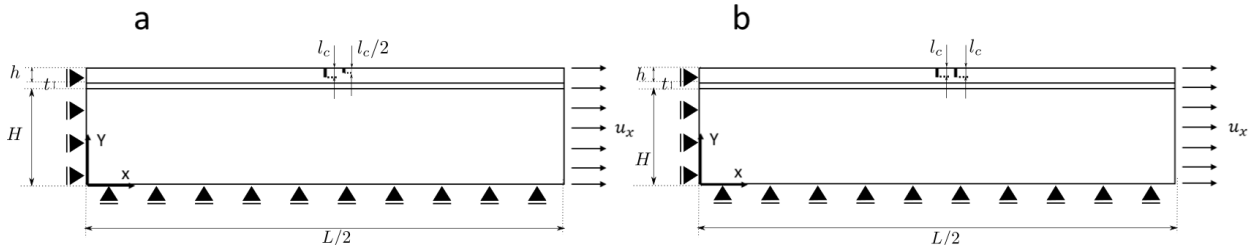

Figure 5: (a) Secondary notch of length equal to $lc/2$. (b) Secondary notch of length equal to lc.

3.1.2. 2D film/substrate system under bending

In the previous problems, the failure corresponded to pure fracture Mode I. In this Section, we extend our study analyzing the systems responses under mixed fracture modes (Mode I and II), which can be introduced by adding a vertical displacement leading to in-plane bending (See Figure 8).

Two problems have been examined: (a) an external solicitation for which the vertical and horizontal displacements are of the same magnitude, and (b) the magnitude of the vertical imposed displacement is the half with respect to that corresponding to the horizontal displacement.

The corresponding simulation results to the solicitations previously identified by (a) and (b) are shown in Figure 9 and 10, respectively. In these graphs it can be seen that in the case of a weak or an intermediate interface, the governing failure is due to thin layer-substrate delamination. However, in the case of a very tough interface, an exclusive propagation through the substrate is predicted with no interaction with any other dissipative mechanism. Finally, from a qualitative standpoint, it can be stated that the particular interface cases herein considered, as the horizontal displacement decreases (Mode I decreases), the stiffness of the system decreases and the final deformation level at the collapsing point increases.

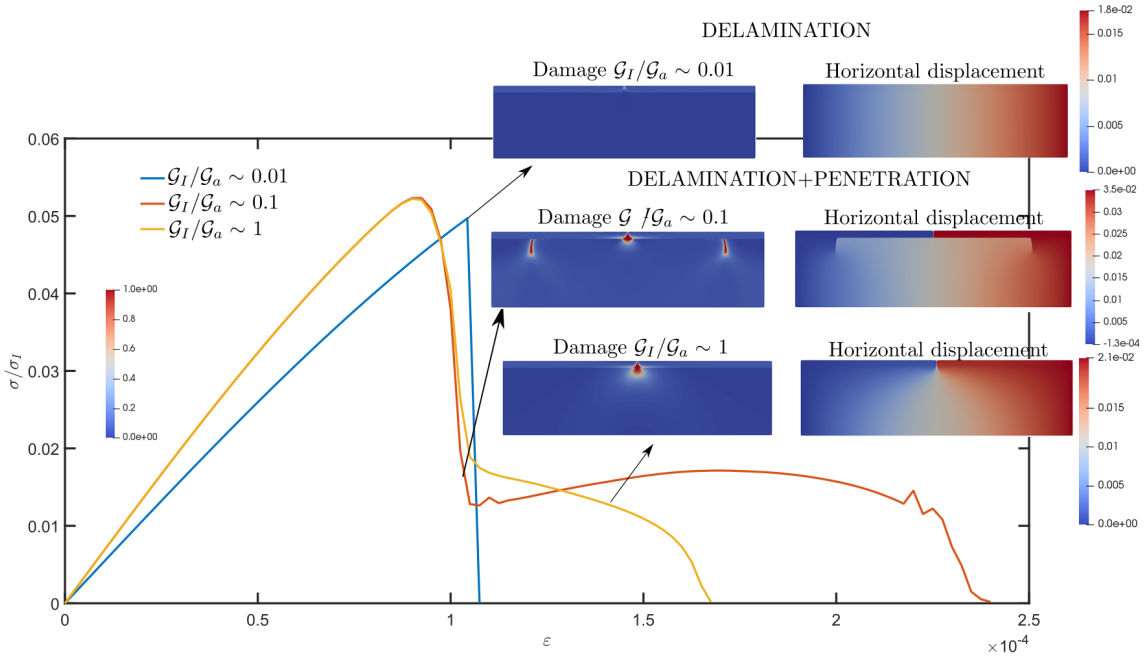

Figure 6: Secondary notch of length equal to $lc/2$: Influence of $\mathcal{G}_I$ on the stress-strain evolution curve.

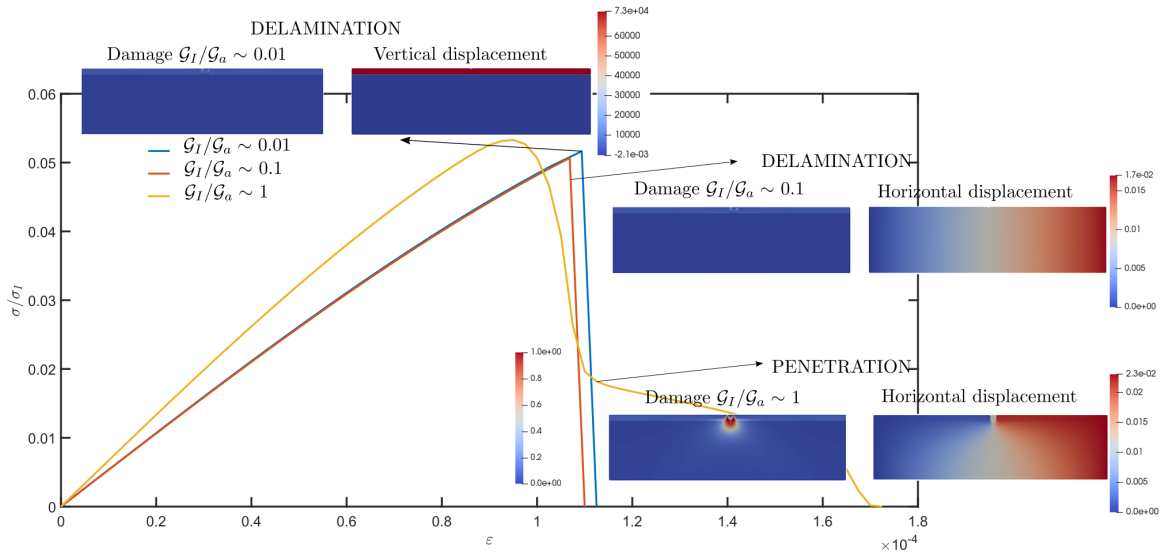

Figure 7: Secondary notch of length equal to lc: Influence of $\mathcal{G}_I$ on the stress-strain evolution curve.

3.1.3. 2D film/substrate system: construction of a potential failure map.

Through the exploitation of the current numerical approach, in this Section, we aim at constructing an overall failure map of the 2D film/substrate system, which is given in Figure 3 for different values of the Dundurs' parameter α, and also different values of $\mathcal{G}_I$. Therefore, knowing the properties of our system, we can easily determine the type of failure that might arise in each particular configuration of the system. This failure map is shown in Figure 11, where we can see that there are three predominant types of failure: (1) delamination ($0.1 \leq \mathcal{G}_I/\mathcal{G}_b \leq 0.25$), (2) delamination+penetration ($0.75 \leq \mathcal{G}_I/\mathcal{G}_b \leq 1$) and (3) penetration

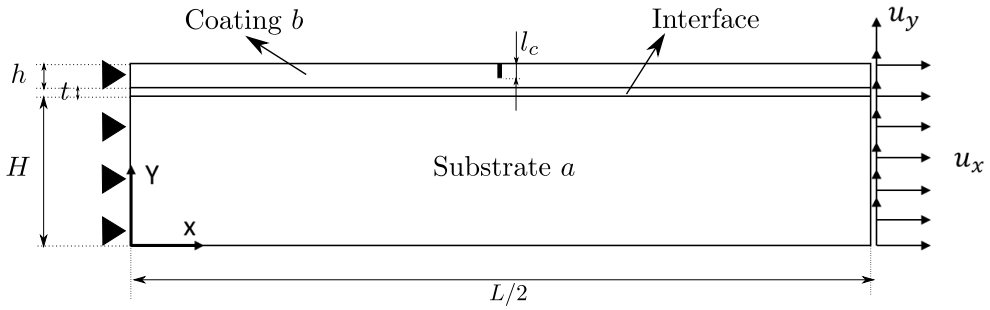

Figure 8: 2D film/substrate under bending: Geometry.

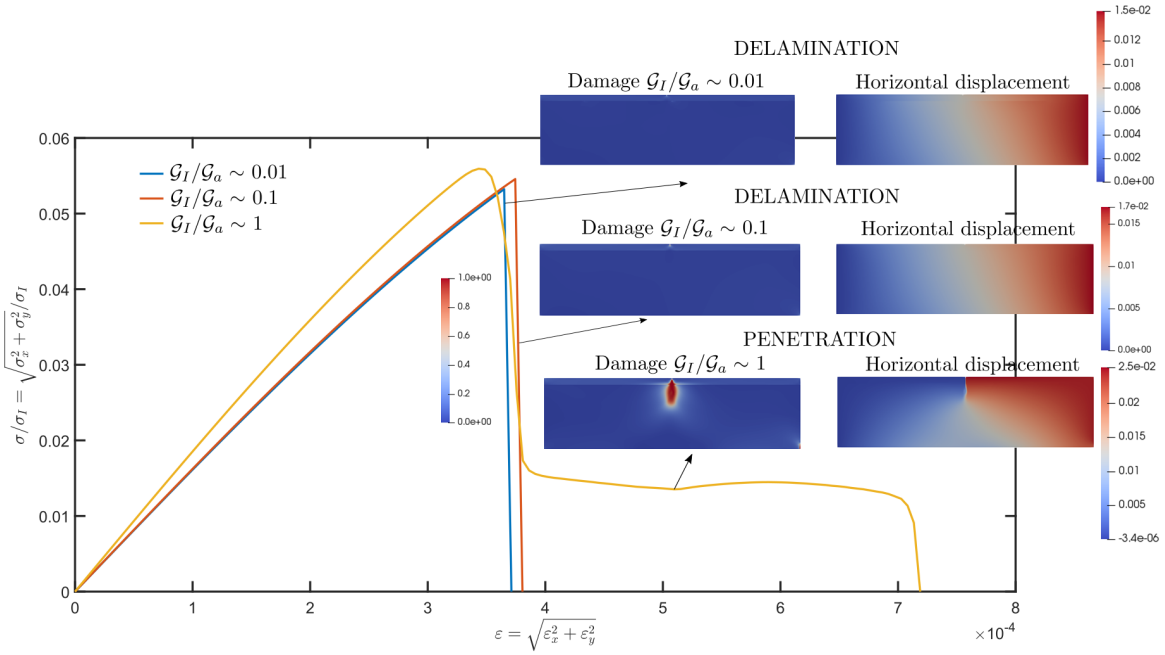

Figure 9: 2D film/substrate system under bending (a): $u_y = -0.005$ and $u_x = 0.005$ mm. Influence of $\mathcal{G}_I$ on the stress-strain evolution curve.

($5 \leq \mathcal{G}_I/\mathcal{G}_b \leq 43$). From this failure map we can elucidate that as α decreases, the damage extent prediction in the substrate increases for all the types of failure.

3.2. 3D film/substrate system.

In this Section, we focus our attention on examining the capability of the proposed method to model 3D applications of thin layer-substrate systems. To do so, we simulate the 3D problem given in Figure 12. The geometry and material parameters are listed in Tables 3 and 4. As can be observed in Figure 12, the geometry is subjected to several loading conditions, so we are simultaneously considering different fracture Modes, i.e. Mode I, II and III in an individual case.

The results of this problem are shown in Figure 13, whereby different failure mechanisms can be identified. Analyzing in detail these results, it can be appreciated that in the weak and intermediate interface cases, the initial predicted failure is due to delamination. Moreover, for the intermediate interface case, it is observable that the corresponding failure pattern shows the concomitant development of delamination and bulk damage,

which is characterized by a notable secondary plateau evolution prior the collapsing point. Differing from this, as can be expected, in the weak interface case, the corresponding failure mode of the system corresponds to the exclusive development of delamination with a single plateau evolution and a subsequent sudden drop. These two failure patterns contrast with that corresponding to the tough interface case, in which the strong

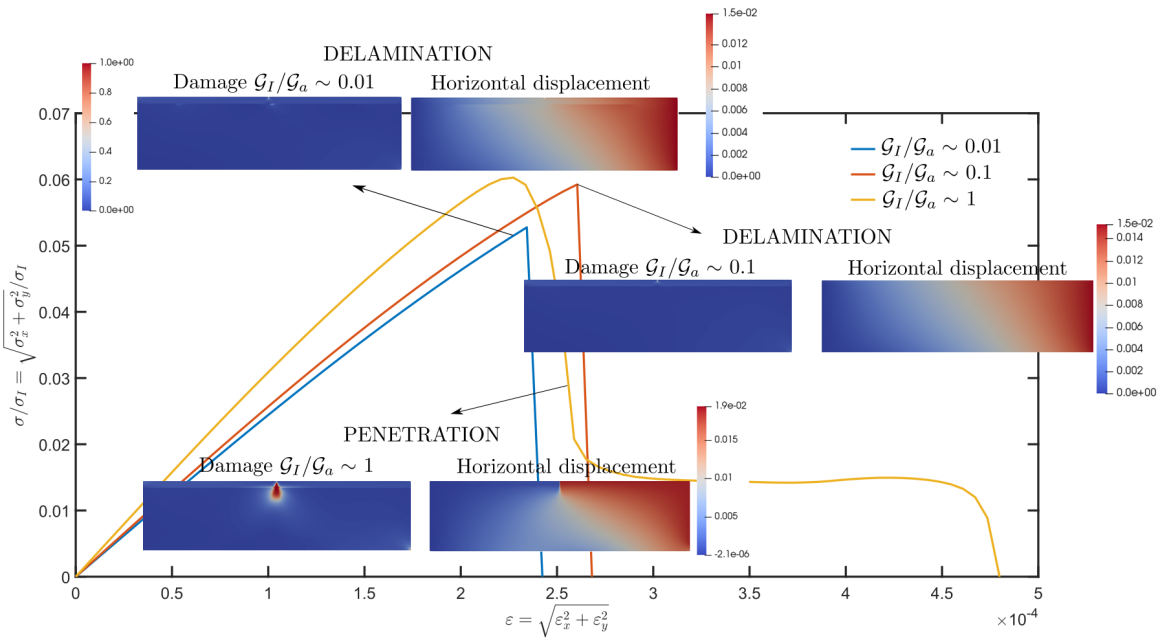

Figure 10: 2D film/substrate system under bending (b): $u_y = -0.005$ mm and $u_x = 0.1$ mm. Influence of $\mathcal{G}_I$ on the stress-strain evolution curve.

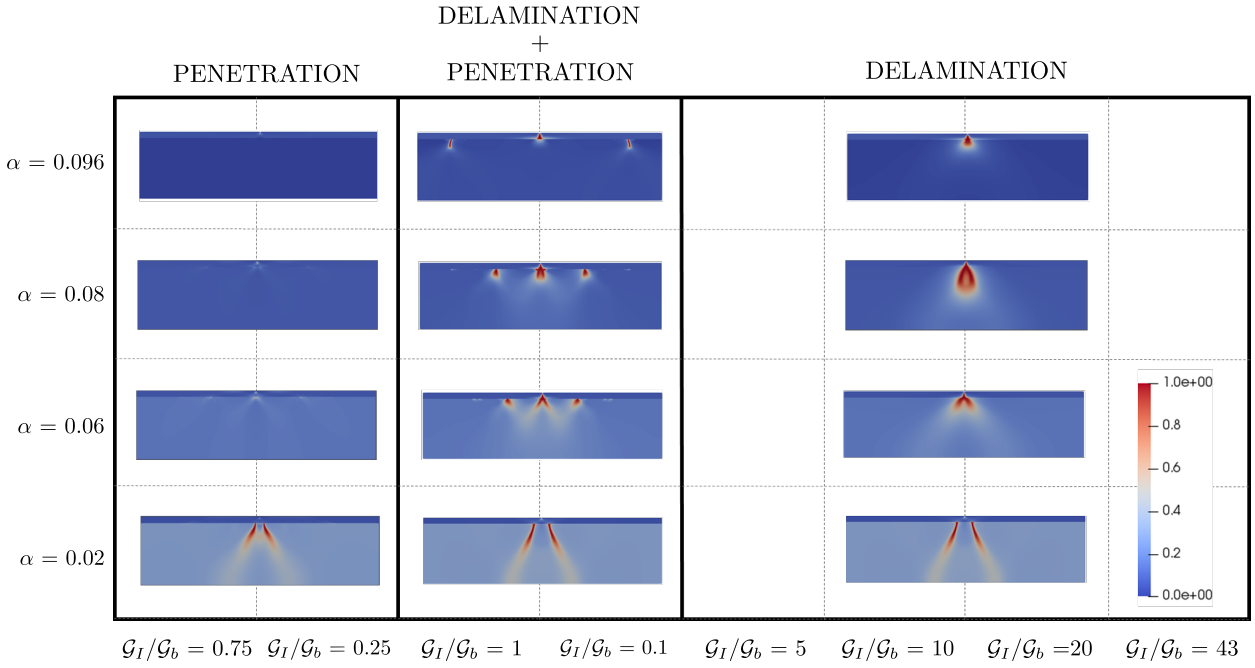

Figure 11: Failure map of the 2D film/substrate system under tension: Dundurs' parameter α vs $\mathcal{G}_I/\mathcal{G}_b$.

energetic barrier of the interface provokes the breakage of the coating and precluding the initiation and evolution of deflection or penetration events along the prescribed the interface.

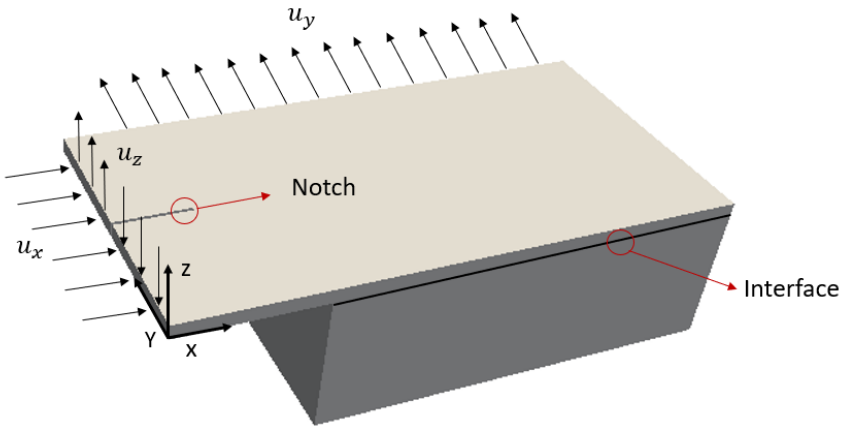

Figure 12: 3D film/substrate system: Geometry.

L/t	2020	Specimen length/Interface thickness
L_a/t	1500	Substrate length/Interface thickness
W/t	1000	Specimen width/Interface thickness
h/t	50	Coating thickness/Interface thickness
H/t	500	Substrate thickness/Interface thickness
l_c/t	12	Notch length/Interface thickness

Table 3: 3D film/substrate system: Geometrical parameters.

$E_a/\mathcal{G}_a$	3.79×10^{4}	Substrate Young modulus/Substrate Fracture energy
$E_b/\mathcal{G}_a$	3.79×10^{5}	Coating Young modulus/Substrate Fracture energy
$\nu_a/\mathcal{G}_a$	11.71	Coating Poisson ratio /Substrate Fracture energy
$\nu_b/\mathcal{G}_a$	11.71	Substrate Poisson ratio/Substrate Fracture energy
$\mathcal{G}_b/\mathcal{G}_a$	2	Coating Fracture energy/Substrate Fracture energy
$l/\mathcal{G}_a$	3.82×10^{-2}	Phase field length scale parameter/Substrate Fracture energy
$\mathcal{G}_{int}/\mathcal{G}_a$	0.17	Interface Fracture energy for Mode I, II and III/Substrate Fracture energy
$\sigma_{int}/\mathcal{G}_a$	2.58×10^{4}	Interface Maximum traction for Mode I, II and III/Substrate Fracture energy
α	0.82	Dundurs' parameter α
β	0.5	Dundurs' parameter β

Table 4: 3D film/substrate system: Mechanical properties.

4. Concluding remarks

In the present work, the problem of fracture and debonding of a thin film bonded on a compliant substrate has been carefully investigated on several thin film-substrate systems with the presence of interfaces from a numerical standpoint. For this purpose, it has been exploited the 2D and 3D phase field model for brittle fracture coupled with the CZM for triggering bulk and interface cracks, respectively, in an efficient and reliable manner. This coupling is performed reducing the stiffness of the CZM with the increasing damage at the surrounding bulk and allows the simulation of delamination on the interface. This model has been

implemented within the nonlinear FEM context for the analysis of plane strain systems and for fully 3D applications through the use of a enhanced assumed the solid shell formulation.

Derived from the current predictions, we have shown the capability of this methodology to simulate 2D and 3D problems and to capture different crack paths depending on the material and fracture properties of the system. In particular, it has been analysed the influence of the interface fracture energy on the type of failure. For instance, in the 2D film substrate system, we illustrated the different failure mechanisms that can experience thin layer-substrate systems based on the interface definition (weak, intermediate or tough) for given bulk properties. Exploiting the versatility and robustness of the current numerical method, current simulations enabled the construction of an overall failure map of such systems depending on the fracture properties and the Dundurs' parameters between the constituents. This yields to very valuable information regarding the different failure patterns that govern the system response. This is a novel contribution in the field, since the current methodology provides a complete failure map, not only analysing the system response around the pre-existing notches and interfaces, but also gives additional information for subsequent propagation into the adjacent substrate upon complete failure.

Relying on the reliability of the present estimations, future developments might regard further analysis on the 3D thin film-substrate systems, in particular with regard to curved geometries. Finally, further work should be conducted to achieve a quantitative-qualitative correlation with respect to experimental data.

References

[1] He Ming-Yuan and John W Hutchinson. Crack deflection at an interface between dissimilar elastic materials. *International Journal of Solids and Structures*, 25(9):1053–1067, 1989.

[2] John W Hutchinson and Zhigang Suo. Mixed mode cracking in layered materials. In *Advances in applied mechanics*, volume 29, pages 63–191. Elsevier, 1991.

[3] Raúl Bermejo and Robert Danzer. High failure resistance layered ceramics using crack bifurcation and interface delamination as reinforcement mechanisms. *Engineering Fracture Mechanics*, 77(11):2126–2135, 2010.

[4] E Martin, D Leguillon, and C Lacroix. A revisited criterion for crack deflection at an interface in a brittle bimaterial. *Composites science and technology*, 61(12):1671–1679, 2001.

[5] D Leguillon, C Lacroix, and E Martin. Interface debonding ahead of a primary crack. *Journal of the Mechanics and Physics of Solids*, 48(10):2137–2161, 2000.

[6] M Ortiz and A Pandolfi. Finite deformation irreversible cohesive elements for three-dimensional crack-propagation analysis. *International Journal for Numerical Methods in Engineering*, 44:1267–1282, 1999.

[7] J Reinoso and M Paggi. A consistent interface element formulation for geometrical and material nonlinearities. *Computational Mechanics*, 54(6):1569–1581, 2014.

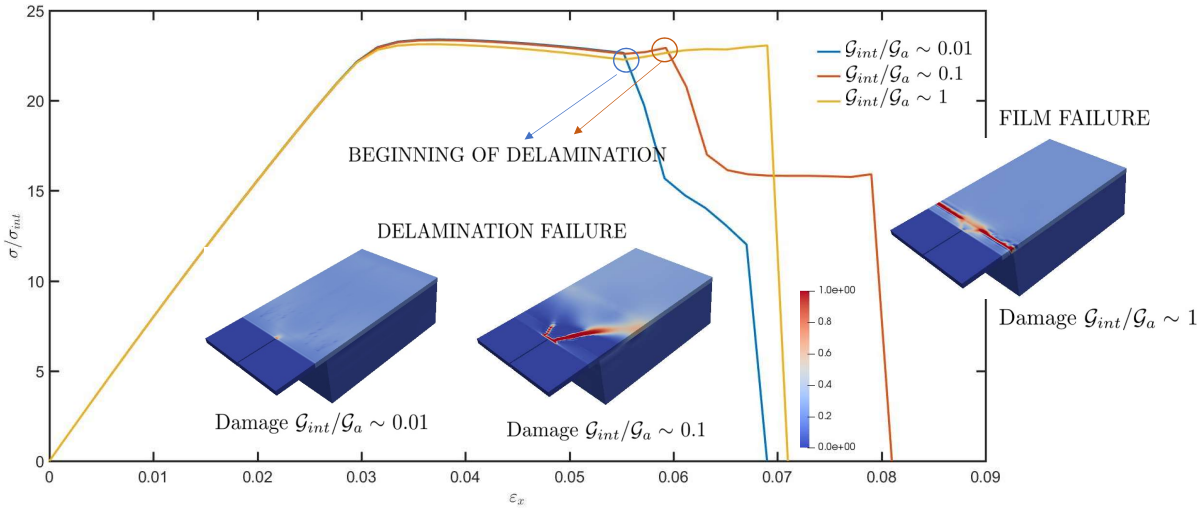

Figure 13: 3D film/substrate system: stress-strain evolution curve and damage pattern.

[8] Haixia Mei, Chad M Landis, and Rui Huang. Concomitant wrinkling and buckle-delamination of elastic thin films on compliant substrates. *Mechanics of Materials*, 43(11):627–642, 2011.
[9] José Reinoso, Marco Paggi, and Raimund Rolfes. A computational framework for the interplay between delamination and wrinkling in functionally graded thermal barrier coatings. *Computational Materials Science*, 116:82–95, 2016.
[10] F Armero and C Linder. New finite elements with embedded strong discontinuities in the finite deformation range. *Computer Methods in Applied Mechanics and Engineering*, 197(33):3138–3170, 2008.
[11] J Dolbow, N Moës, and T Belytschko. An extended finite element method for modeling crack growth with frictional contact. *Computer methods in applied Mechanics and engineering*, 190(51):6825–6846, 2001.
[12] GA Francfort and J-J Marigo. Revisiting brittle fracture as an energy minimization problem. *Journal of the Mechanics and Physics of Solids*, 46(8):1319–1342, 1998.
[13] B Bourdin, GA Francfort, and J-J Marigo. The variational approach to fracture. *Journal of elasticity*, 91(1):5–148, 2008.
[14] C Miehe, M Hofacker, and F Welschinger. A phase field model for rate-independent crack propagation: Robust algorithmic implementation based on operator splits. *Computer Methods in Applied Mechanics and Engineering*, 199(45):2765–2778, 2010.
[15] L Ambrosio and VM Tortorelli. Approximation of functional depending on jumps by elliptic functional via t-convergence. *Communications on Pure and Applied Mathematics*, 43(8):999–1036, 1990.
[16] M Hofacker and C Miehe. A phase field model of dynamic fracture: Robust field updates for the analysis of complex crack patterns. *International Journal for Numerical Methods in Engineering*, 93(3):276–301, 2013.
[17] C Miehe, LM Schänzel, and H Ulmer. Phase field modeling of fracture in multi-physics problems. part i. balance of crack surface and failure criteria for brittle crack propagation in thermo-elastic solids. *Computer Methods in Applied Mechanics and Engineering*, 294:449–485, 2015.
[18] C Miehe, M Hofacker, L-M Schaenzel, and F Aldakheel. Phase field modeling of fracture in multi-physics problems. part ii. coupled brittle-to-ductile failure criteria and crack propagation in thermo-elastic–plastic solids. *Computer Methods in Applied Mechanics and Engineering*, 294:486–522, 2015.
[19] F Amiri, D Millán, Y Shen, T Rabczuk, and M Arroyo. Phase-field modeling of fracture in linear thin shells. *Theoretical and Applied Fracture Mechanics*, 69:102–109, 2014.
[20] P Areias, T Rabczuk, and MA Msekh. Phase-field analysis of finite-strain plates and shells including element subdivision. *Computer Methods in Applied Mechanics and Engineering*, 312:322–350, 2016.
[21] J Reinoso, M Paggi, and C Linder. Phase field modeling of brittle fracture for enhanced assumed strain shells at large deformations: formulation and finite element implementation. *Computational Mechanics*, pages 1–21, 2017.
[22] Emilio Martínez-Pañeda, Alireza Golahmar, and Christian F Niordson. A phase field formulation for hydrogen assisted cracking. *Computer Methods in Applied Mechanics and Engineering*, 342:742–761, 2018.
[23] M Paggi and J Reinoso. Revisiting the problem of a crack impinging on an interface: a modeling framework for the interaction between the phase field approach for brittle fracture and the interface cohesive zone model. *Computer Methods in Applied Mechanics and Engineering*, 321:145–172, 2017.
[24] M Paggi, M Corrado, and J Reinoso. Fracture of solar-grade anisotropic polycrystalline silicon: A combined phase field–cohesive zone model approach. *Computer Methods in Applied Mechanics and Engineering*, 330:123–148, 2018.
[25] V Carollo, J Reinoso, and M Paggi. A 3d finite strain model for intralayer and interlayer crack simulation coupling the phase field approach and cohesive zone model. *Composite Structures*, 182:636–651, 2017.
[26] V Carollo, J Reinoso, and M Paggi. Modeling complex crack paths in ceramic laminates: A novel variational framework combining the phase field method of fracture and the cohesive zone model. *Journal of the European Ceramic Society*, 38(8):2994–3003, 2018.
[27] CV Verhoosel and R Borst. A phase-field model for cohesive fracture. *International Journal for numerical methods in Engineering*, 96(1):43–62, 2013.
[28] JG Williams and H Hadavinia. Analytical solutions for cohesive zone models. *Journal of the Mechanics and Physics of Solids*, 50(4):809–825, 2002.
[29] Luis Távara, José Reinoso, David Castillo, and Vladislav Mantič. Mixed-mode failure of interfaces studied by the 2d linear elastic–brittle interface model: Macro-and micro-mechanical finite-element applications in composites. *The Journal of Adhesion*, 94(8):627–656, 2018.
[30] J Reinoso and A Blázquez. Application and finite element implementation of 7-parameter shell element for geometrically nonlinear analysis of layered cfrp composites. *Composite structures*, 139:263–276, 2016.
[31] J. Reinoso and A. Blzquez. Geometrically nonlinear analysis of functionally graded power-based and carbon nanotubes reinforced composites using a fully integrated solid shell element. *Composite Structures*, 152:277 – 294, 2016.
[32] M Bischoff and E Ramm. Shear deformable shell elements for large strains and rotations. *International Journal for Numerical Methods in Engineering*, 40(23):4427–4449, 1997.
[33] S Klinkel and W Wagner. A geometrical non-linear brick element based on the eas-method. *International Journal for Numerical Methods in Engineering*, 40(24):4529–4545, 1997.
[34] M Paggi and P Wriggers. Stiffness and strength of hierarchical polycrystalline materials with imperfect interfaces. *Journal of the Mechanics and Physics of Solids*, 60(4):557–572, 2012.
[35] Erwan Tanné, Tianyi Li, Blaise Bourdin, J-J Marigo, and Corrado Maurini. Crack nucleation in variational phase-field models of brittle fracture. *Journal of the Mechanics and Physics of Solids*, 110:80–99, 2018.
[36] JP Parmigiani and MD Thouless. The roles of toughness and cohesive strength on crack deflection at interfaces. *Journal of the Mechanics and Physics of Solids*, 54(2):266–287, 2006.